Osteogenic differentiation of hBMSCs on porous photo-crosslinked poly (trimethylene carbonate) and nano-hydroxyapatite composites☆

Mike A. Geven [a,1], Anna Lapomarda [b,c], Olivier Guillaume [d,2], Christoph M. Sprecher [d], David Eglin [a,d,3], Giovanni Vozzi [b,c], Dirk W. Grijpma [a,*]

[a] *MIRA Institute for Biomedical Technology and Technical Medicine, and Department of Biomaterials Science and Technology, University of Twente, P.O. Box 217, 7500 AE Enschede, The Netherlands*
[b] *Research Center "E. Piaggio", University of Pisa, Via Diotisalvi, 1, 56122 Pisa, Italy*
[c] *Dipartimento di Ingegneria dell'Informazione, University of Pisa, Via Girolamo Caruso, 16, 56122 Pisa, Italy*
[d] *AO Research Institute Davos, Clavadelerstrasse 8, 7270 Davos, Switzerland*

ARTICLE INFO

ABSTRACT

Large bone defects are challenging to repair and novel implantable materials are needed to aid in their reconstruction. Research in the past years has proven the beneficial effect of porosity in an implant on osteogenesis *in vivo*. Building on this research we report here on porous composites based on photo-crosslinked poly(trimethylene carbonate) and nano-hydroxyapatite. These composites were prepared by a temperature induced phase separation of poly(trimethylene carbonate) macromers from solution in ethylene carbonate. By controlling the ethylene carbonate content in viscous dispersions of nano-hydroxyapatite in poly(trimethylene carbonate) macromer solutions, composites with 40 wt% nano-hydroxyapatite and 27 to 71% porosity were prepared. The surface structure of these porous composites was affected by their porosity and their topography became dominated by deep micro-pore channels with the majority of pore widths below 20 μm and rougher surfaces on the nano-scale. The stiffness and toughness of the composites decreased with increasing porosity from 67 to 3.5 MPa and 263 to 2.2 N/mm^2, respectively. In cell culture experiments, human bone marrow mesenchymal stem cells proliferated well on the composites irrespective of their porosity. Furthermore, differentiation of the cells was demonstrated by determination of ALP activity and calcium production. The extent of differentiation was affected by the porosity of the films, offering a reduced mechanical incentive for osteogenic differentiation at higher porosities with topographies likely offering a reduced possibility for cells to aggregate and to elongate into morphologies favourable for osteogenic differentiation. This ultimately resulted in a 3-fold reduction of calcium production of the differentiated cells on composites with 71% porosity compared to those on composites with 27% porosity.

1. Introduction

In recent years *in vitro* and *in vivo* research in bone tissue engineering has increased the understanding of factors controlling the clinical outcome of reconstruction. It is known which size features are desired for the porosity of an implant [1–6], which surface micro- and nano-structure is efficacious [7–14], and how the mechanical properties [15–17] affect the osteogenicity and –integration of an implant. In practice several of these factors are interrelated and compromises are generally made, such as those between the mechanical properties and

* Corresponding author.
E-mail addresses: mike.geven@iit.it (M.A. Geven), anna.lapomarda@ing.unipi.it (A. Lapomarda), olivier.guillaume@tuwien.ac.at (O. Guillaume), christoph.sprecher@aofoundation.org (C.M. Sprecher), david.eglin@emse.fr (D. Eglin), g.vozzi@ing.unipi.it (G. Vozzi), d.w.grijpma@utwente.nl (D.W. Grijpma).
[1] Author's current address: Istituto Italiano di Tecnologia, Laboratory of Polymers and Biomaterials, Via Morego 30, 16163 Genova, Italy.
[2] Author's current address: Technische Universität Wien, Research Group for 3D Printing and Biofabrication, Getreidemarkt 9, 1060 Wien, Austria.
[3] Author's current address: Mines Saint-Etienne, Univ Lyon, Univ Jean Monnet, INSERM, U 1059 Sainbiose, Centre CIS, F-42023 Saint-Etienne, France.

the porosity[18,19].

A multitude of techniques has been developed for a controlled modification of implant materials in order to obtain desired porosities, mechanical properties or surface roughness. Among these, the formation of composites is frequently explored for reinforcement and surface roughening of polymeric systems or toughening of inorganic ones, allowing for facile optimization by simple adjustment of the component ratios[20–22]. Surface treatments are commonly applied to enhance roughness of materials on the nano-scale, which in combination with a microscale roughness, can improve cell adhesion and promote osteogenic differentiation[8,9,23]. Techniques that are regularly employed include atmospheric plasma[24,25] or alkaline treatments[26]. When carefully optimized, these treatments have the added benefit that mechanical properties and porosity remain unaffected. Similarly, coatings such as collagen[27], gelatin/hydroxyapatite composites[28] or plasma polymerized acrylamides[29] are applied to enhance cell adhesion or differentiation. In recent works, alkaline phosphatase (ALP) coatings were employed to initiate surface mineralization of implant materials through the enzyme's activity, therewith enhancing surface roughness [30,31]. Porosity has generally been obtained by use of porogens such as salts[32], sugars[33] or solvent crystals following temperature-induced phase separation (TIPS)[34]. More recent progress in the formation of porous implants has demonstrated that additive manufacturing techniques allow for preparation of well-defined and interconnected porosities[32,35] or that the combination of porogen leaching and additive manufacturing allows for formation of structures with porosity on different size scales[36,37]

The effect of porosity of implant materials on the clinical outcome of bone reconstruction has been researched extensively. The porosity of the implant material is essential for ingrowth of bone tissue and to allow for vascularization[18,19,38–40]. Porosity can additionally improve *de novo* bone ingrowth by enhancing the roughness of the implant, increasing the local protein concentration and by improving nutritional supply to the *de novo* bone that has grown into the implant[40–42]. The mechanical properties of the implant are of functional importance in bone restoration as adequate mechanical properties allow for the implant to act as a temporary support structure. Moreover, the osteogenic differentiation of osteoprogenitor cells is enhanced on materials with increasing stiffness[15,16,43]. Given the compromise between porosity and mechanical properties, these factors need to be balanced for effective restoration of a bony defect.

In previous work we reported on composite materials of photo-crosslinked poly(trimethylene carbonate) (PTMC) and 40 wt% nano-hydroxyapatite (nHA), prepared by additive manufacturing (stereolithography). These materials have a completely interconnected, designed porosity and high surface roughness due to enrichment of the surface with nHA. They therefore allow for good cell proliferation and differentiation on their surfaces *in vitro,* they enhance reconstruction of calvarial defects *in vivo* in rabbits[35,44] and allow for orbital floor restoration in sheep[45]. In other work we have used extrusion-based additive manufacturing and a temperature induced phase separation method to prepare photo-crosslinked PTMC/nHA composites with a multi-scale porosity[37]. Ethylene carbonate (EC, melting point 36 °C) was used to dissolve the photo-crosslinkable polymer phase and disperse nHA at elevated temperatures. By controlled spatial deposition of the resulting resin at reduced temperatures, 3D structures with a designed porosity on the macro-scale (>300 μm) were prepared with entrapped solvent crystals. These crystals were extracted after photo-crosslinking of the PTMC/nHA matrix, resulting in an additional micro-scale porosity (less than 20 μm) in the struts of the structure. The rationale behind these structures is that the macro-scale porosity allows for tissue infiltration following implantation, whereas the microporosity is too small for infiltration and functions as conduit for waste removal and nutrient supply.

The micro-scale porosity may have a profound effect on the surface structure of the struts and on cell-material interaction, however. In this work we therefore use a 2D model of these composites possessing a micro-scale porosity generated by TIPS. By varying the concentration of EC in the resins of photo-crosslinkable PTMC and nHA, we are able to adjust porosity, surface topography and mechanical properties of the resulting composites while keeping the nHA content (40 wt%) more or less constant. We furthermore show the effect of the porosity on calcium release and protein adhesion as these factors may play an important role in bone restoration[44,46,47] and the various porous composites are subjected to adhesion, proliferation and osteogenic differentiation assays with human bone marrow mesenchymal stem cells (hBMSCs) as indicators of cell-material interaction.

The fabrication method described here can be used to optimize composite materials for bone tissue engineering as it allows for direct attuning of the porosity and mechanical properties by only controlling the solvent concentration and fabrication temperatures during composite preparation.

2. Materials & methods

2.1. Materials

Hiuzhou ForYou Medical Devices Ltd. provided the trimethylene carbonate (TMC) used. Tin(II) 2-ethylhexanoate ($Sn(Oct)_2$), 1,1,1-tris(hydroxymethyl)propane (TMP), hydroquinone (HQ), methacrylic anhydride, triethylamine, ethylene carbonate, formic acid ($\geq$95.5%), sodium hydrogen carbonate, ascorbic acid, glycerol-2-phosphate (disodium salt hydrate), dexamethasone, phosphatase substrate, alkaline buffer solution (1.5 M, pH 10.3), Live/Dead® staining reagents, alizarin red staining (ARS, 40 mM) solution, bovine serum albumin and a calcium colorimetric assay kit (MAK022) were acquired from Sigma Aldrich. Omnirad TPO-L photo-initiator was obtained from IMG Resins BV. Kuros Biosciences BV provided nHA in the form of a powder with aggregates (Ø = 15 μm) of needle-like hydroxyapatite crystals of 200 to 400 nm long and 20 to 50 nm wide.

Tris(hydroxymethyl) aminomethane hydrochloride salt (Tris-HCL, > 99%), diethanolamine and hexamethyldisilazane (HMDS) were obtained from Carl Roth GmbH. Dulbecco's modified eagle medium (DMEM, low glucose, pyruvate) powder, minimum essential medium α (α-MEM) and penicilin streptomycin (10,000 U/ml) were from Gibco. SeraPlus serum was acquired from Milan Analytica AG. A Quick Start™ Bradford Protein Assay was from Bio-Rad. A CellTiter-Blue® assay was acquired from Promega and a CyQuant™ cell proliferation assay kit was used from Invitrogen. Nunc™ Thermanox™ coverslips were obtained from Thermofisher.

Dichloromethane was from VWR International and was dried over calcium hydride and subsequently distilled under a dry N_2 atmosphere. Other materials were used as received unless stated otherwise. Water used for this work was either deionized (DI) water or ultrapure (UP) water purified by a MilliQ® Reference system. Phosphate buffered saline (PBS) used in this work was a 0.01 M phosphate buffer at pH 7.4.

2.2. Synthesis of photo-crosslinkable PTMC

Three-armed methacrylate end-group functionalized poly(trimethylene carbonate) (PTMC-MA) was synthesized as previously described[48]. Briefly, a three-armed TMC oligomer was prepared by ring-opening polymerization of TMC initiated by TMP using $Sn(Oct)_2$ (0.13 wt%) as a catalyst (molar ratio TMC/TMP = 96.2). The polymerization reaction was conducted for three days at 130 °C under N_2 atmosphere. Thereafter the oligomer was dissolved in dry dichloromethane under N_2. To this solution HQ at 0.1 wt% relative to TMC oligomer, triethylamine (9 mol/mol TMC oligomer) and methacrylic anhydride (9 mol/mol TMC oligomer) was subsequently added under stirring to functionalize the oligomer with methacrylate end-groups. The functionalization was left to proceed for 5 days at room temperature under N_2 atmosphere. The resulting solution was precipitated in ice-

cooled methanol and the precipitate was additionally extracted in ice-cooled methanol for 2 h. It was thereafter dried *in vacuo* at room temperature until constant weight. The resulting macromer was analysed by ^{1}H NMR (Bruker Ascend 400/Avance III 400 MHz NMR spectrometer) to determine the molar mass and degree of functionalization as was described previously[49]. Deuterated chloroform was used as a solvent for ^{1}H NMR.

2.3. Preparation of resins and composite films

Resins to produce porous composite films were prepared by adding nHA and PTMC-MA into chloroform at a weight ratio of 0.67 (nHA/PTMC-MA). The concentration of PTMC-MA was 0.1 g/ml. This mixture was stirred overnight in the dark to dissolve the PTMC-MA. The resulting dispersion was co-precipitated in ice-cooled methanol and the collected precipitate was dried *in vacuo* until constant weight. After drying, the precipitate was mixed with a calculated amount of EC at 50 °C for two days in the dark. This mixture was sonicated at 50 °C for 30 min and HQ at 0.1 wt% relative to PTMC-MA and Omnirad TPO-L at 5 wt% relative to PTMC-MA were mixed-in directly after.

Three different concentrations of EC (35, 60 and 85 vol% of the total resin composition) were used in order to prepare resins for the production of films with 35, 60 and 85% porosity (LowEC, MidEC and HighEC respectively). The final concentration of all components in these three resins is depicted in table 1.

Porous composite films were prepared by casting resins at a thickness of 0.5 mm on a heated glass plate. The glass plate was then cooled for 2 h in a refrigerator or freezer to induce a phase separation. The casting and cooling temperatures applied are given in table 2. As the concentration of EC in the resins influenced the rate of EC crystallization and the size of EC crystals, these temperatures were adjusted to control the cooling rate. Films were then photo-crosslinked in a UV-crosslinking box at 365 nm and 11 mW/cm^2 under N$_2$ atmosphere for 30 min at room temperature. The EC was thereafter extracted in deionized water for 24 h and subsequently in a mixture of ethanol and propylene carbonate (1/1 v/v) which was exchanged to pure ethanol stepwise. The films were subsequently dried under ambient conditions for 3 days. The thickness of the dried films was between 0.30 and 0.45 mm.

2.4. Characterization of resins and porous composite films

Melting- and crystallization temperatures of the resins were determined by differential scanning calorimetry (DSC) using a Perkin Elmer Pyris 1 differential scanning calorimeter. Samples (n = 3) were heated from −45 to 75 °C under N$_2$ atmosphere using a heating rate of 5 °C/minute. Subsequently the samples were kept at 75 °C for 30 min after which they were cooled to −45 °C at a rate of 5 °C/minute. The samples were kept at −45 °C for 30 min after which a second, identical heating and cooling cycle was performed. The melting temperature of the resins was determined as the peak temperature of the first heating cycle, whereas the crystallization temperature was determined as the peak temperature in the second cooling cycle.

The viscosity of the resins was determined by rheology on an Anton Paar Physica MCR-201 rheometer equipped with PP25 measurement probe with a 25 mm diameter. Measurements were performed at the

Table 1

Composition of resins used for this work.

Component	Resins		
	LowEC	MidEC	HighEC
PTMC-MA (wt.%)	41.5	28.1	11.1
nHA (wt.%)	27.7	18.7	7.4
EC (wt.%)	28.7	51.8	81.0
Omnirad TPO-L (wt.%)	2.1	1.4	0.5
HQ (wt.%)	4·10^{-2}	3·10^{-2}	1·10^{-2}

Table 2

Temperatures applied for resin casting and for cooling.

Applied temperature	Resins		
	LowEC	MidEC	HighEC
Casting (°C)	50	50	40
Cooling (°C)	−25	4	4

casting temperatures of the resins and a measurement gap of 0.3 mm. Preliminary experiments demonstrated the resins to be shear thinning with a sharp drop in viscosity at shear rates from 0.01 to 10 s^{-1}. To avoid reorientation of nHA particles and its possible aggregates causing fluctuations in the measured viscosity, samples were equilibrated in the low viscosity region of the resins by a pre-shear of 10 s^{-1} for 5 min and were thereafter equilibrated at 0.01 s^{-1} for 2 min to match the initial measurements conditions. The shear rate was thereafter increased from 0.01 to 100 s^{-1} at 30 points per decade and 6 s in-between measuring points.

The surface and cross-sections of freeze-fractured films were visualized using a Zeiss Merlin high resolution scanning electron microscope (HR-SEM) equipped with a high efficiency scanning electron detector at 1.4 to 5 kV. Pore width was determined from the SEM images by ImageJ. At least 300 randomly selected pores per film were analysed and for each pore, widths were measured at 3 locations along its length. A Welch's two-tailed *t*-test was used to assess significant differences in the pore size distributions, setting the minimum significance level to 0.1

The surface of the films was further characterized by atomic force microscopy (AFM) using a Multi Mode atomic force microscope from Veeco. Images were acquired at ambient conditions on dry, 1x1 cm^2 samples in tapping mode at 1.01 Hz and a scan angle of 90°. The mean roughness (R$_a$, the average deviation of the sample surface height from its mean height) as well as the root mean square roughness (R$_q$, the standard deviation of the sample surface height, which is more sensitive to large variations in sample surface height) were calculated as defined in literature[50].

The nHA content of the composite films was determined by thermogravimetric analysis (TGA) using a Perkin Elmer TGA 7. Samples (n = 3) were heated under N$_2$ flow from 50 to 600 °C at a heating rate of 20 °C/minute. The nHA content was determined from the residual mass of the sample at 600 °C.

To calculate the porosity of the composite films, samples (n = 3, ø = 6 mm) were die-cut from the films and their weight (m$_s$) and thickness was determined. The volumetric porosity (P) in % was thereafter calculated using (1), where f$_{PTMC}$ and f$_{nHA}$ are the weight fractions of PTMC and nHA respectively as was determined by TGA. The densities of PTMC-MA (1.31 g/cm^3) and nHA (3.162 g/cm^3) are ρ$_{PTMC}$ and ρ$_{nHA}$ respectively and V$_s$ is the overall volume of the sample in cm^3 as was determined from its diameter and thickness.

$$P = \left[1 - \frac{m_s}{(f_{PTMC}*\rho_{PTMC} + f_{nHA}*\rho_{nHA})V_s}\right]*100\% \qquad (1)$$

The mechanical properties of the composite films were determined in tensile tests on a Zwick Z020 tensile tester equipped with a 500 N load cell. Film samples (at least n = 5) were die-cut into 100x5 mm^2 strips. An initial grip-to-grip separation of 50 mm and a crosshead speed of 50 mm/minute were applied during sample elongation at ambient conditions. Engineering stress–strain curves were obtained and the E-modulus was determined between 0 and 2% strain. Furthermore, the yield point, ultimate strength and ultimate strain were determined. Additionally, the toughness was determined from the area under the stress–strain curves.

Calcium release from the porous composite films was determined using square samples (n = 3) of 1x1 cm^2. These were incubated in an acidic formic acid buffer containing 133 mM NaCl (pH = 4.5 ± 0.05) at 37 °C for an accelerated release. At selected time points the release medium was completely replaced by fresh medium. To determine the calcium content in the removed medium, a calcium colorimetric assay kit was used according to the supplier's protocol. After treatment by the

assay kit, calcium ion concentration was determined by absorbance at 560 nm.

Protein adsorption on the porous composite films was investigated by incubation of film samples (n = 4, ø = 1.1 cm) in PBS containing 10% (v/v) SeraPlus and 0.02% (w/v) sodium azide at 37 °C for 5 days. Samples were thereafter washed with DI water and mixed with 0.05% (v/v) Triton™ X-100 in UP water for 30 min at room temperature. The resulting supernatant was diluted 5x with DI water to reduce the Triton™ X-100 concentration to 0.01% (v/v). Subsequent analysis was performed using a Quick Start™ Bradford Protein Assay according to the supplier's protocol. Protein concentration was quantified by absorbance at 595 nm after treatment by the assay kit, using bovine serum albumin as a reference to construct a standard curve of protein concentration versus absorbance.

Absorbance was recorded on a Viktor[3] microplate reader of Perkin-Elmer for calcium and protein assays.

2.5. In vitro culture and differentiation of hBMSCs

The hBMSCs used for this work were obtained from vertebral body bone aspirates of two separate donors (undergoing spinal fusion; obtained with informed consent and full ethical approval [KEK Bern 126/03]) as described previously[44,51]. Before seeding, hBMSCs of both donors were expanded separately in α-MEM medium containing 10% (v/v) of SeraPlus.

Disk-shaped composite film samples covering the bottom of wells-plates (96 wells, ϕ = 6.4 mm) were used in cell culture experiments. The film samples were sterilized using a cold ethylene oxide gas treatment (pre-conditioning at 70% relative humidity overnight, followed by vacuum for 3 h and subsequent application of an ethylene oxide/CO_2 gas mixture containing 90% ethylene oxide for 6 h; all stages at 45 °C) and were thereafter kept under vacuum for 5 days until use. Tissue culture polystyrene (TCPS) and Thermanox™ coverslips were used as positive controls in some experiments (24 wells, ϕ = 16 mm were used for the Thermanox™ coverslips). Before seeding the hBMSCs, a pre-incubation of the samples and controls was performed overnight in full osteogenic medium (OM) consisting of a solution of DMEM powder (1 g/ml), sodium hydrogen carbonate (4 mg/ml), penicilin streptomycin (1% [v/v]), SeraPlus (10% [v/v]), ascorbic acid (50 μg/ml), dexamethasone (10 nM) and glycerol-2-phosphate (5 mM) in UP water.

Pre-incubation and the culture of cells of both donors in OM were performed at 37 °C, 5% CO_2 and 90% relative humidity. The cells of both donors were seeded separately at a density of $21 \cdot 10^3$ cells/cm^2 unless stated otherwise. Medium was exchanged twice per week.

An adhesion assay of hBMSCs on film samples (n = 3) was performed by seeding hBMSCs at a density of $135 \cdot 10^3$ cells/cm^2 in 30 μl of OM. Samples were then incubated for 15, 30 and 60 min under cell culture conditions without further addition of medium. The cells were thereafter lysed by incubation at 4 °C for 2.5 h in cell lysis buffer consisting of Triton™ X-100 at 0.1% (v/v) and Tris-HCl at 10 mM (pH 7.4) in DI water. Cell lysates were stored at −80 °C and analysed after thawing, using a CyQuant™ cell proliferation kit according to the supplier's protocol.

The metabolic activity of the hBMSCs was monitored using a Cell-Titer-Blue® assay. At designated time points, seeded samples were washed and incubated in a CellTiter-Blue® solution in OM at 20% (v/v) for 3 h under cell culture conditions. The incubated CellTiter-Blue® solution was thereafter analysed according to the supplier's recommendations.

A Live/Dead® staining was performed after 1 and 28 days of culture. Seeded film samples (n = 2) were incubated for 1 h under cell culture conditions in OM containing Live/Dead® staining reagents (calcein acetoxymethyl ester and ethidium homodimer at 10 and 1 μg/ml respectively). Stained cells were thereafter imaged using a Zeiss Axiovert 200 m fluorescent confocal microscope equipped with an Axiocam HRc.

After 28 days of culture, cells on samples (n = 2) were visualized by SEM. Cells were fixated overnight using a 4% (w/v) buffered para-formaldehyde solution at 4 °C. The samples were subsequently dehydrated by ethanol/DI water mixtures which were slowly exchanged to 100% ethanol. Thereafter samples were treated by mixtures of ethanol/HMDS which were exchanged to 100% HMDS. Following the HMDS treatment the samples were dried under ambient conditions for 3 days, sputter-coated with a gold–palladium layer and imaged using a Hitachi S4700 FESEM at 3 kV.

The ALP activity of hBMSCs was determined after incubation of seeded samples (n = 3) in cell lysis buffer (v.s.). Cell lysates were stored at −80 °C and after thawing the lysates were mixed with DI water, alkaline buffer solution and a phosphatase substrate buffer (25 mg/ml in 1 M diethanolamine buffer with 0.5 mM magnesium chloride in DI water, final pH 9.8). The resulting mixtures were incubated at 37 °C for exactly 15 min and thereafter diluted two-fold with a 0.1 M NaOH solution. Reference solutions of 0 to 700 μM p-nitrophenol in cell lysis buffer were identically treated as reference. The resulting solutions were analyzed by absorbance at 405 nm. Another part of the cell lysates was used for DNA quantification by CyQuant® as described (v.s.). ALP activity was expressed as enzyme activity in mol per minute of incubation time per g of DNA content.

Calcium production by the cells was quantified by ARS. Cells on samples (n = 3) were fixated with a 4% (w/v) formaldehyde solution at room temperature for 15 min. The samples were thereafter incubated with ARS solution at pH 4.2 for 1 h at room temperature. Samples were subsequently washed with DI water for 5 days to remove unbound ARS. The remaining staining was extracted using a 10% (v/v) solution of acetic acid for 30 min at room temperature. The supernatant was heated to 85 °C for 10 min and subsequently cooled on ice. After centrifugation the supernatant was treated by ammonium hydroxide to a pH of 4.1–4.5. Absorbance of the resulting solutions was recorded at 405 nm. ARS concentrations were determined using reference solutions of 0–2000 mM ARS in an acetic acid and ammonium hydroxide buffer at pH 4.3. Negative control samples without cells were treated identically and their ARS content was subtracted from the ARS content of seeded samples.

For all assays the absorbance or fluorescence was measured on a Viktor[3] microplate reader of Perkin-Elmer. All results of cell culture and differentiation experiments are expressed as a pooled average ± standard deviation of both donors. A Welch's two-tailed t-test (n = 3) was used to assess significance, setting the significance level to 0.1.

3. Results & discussion

3.1. Resins and porous composites

Composite resins were prepared from mixtures of PTMC-MA, nHA and EC. Using ^{1}H NMR (supplementary information, figure SI1) it was determined that the PTMC-MA macromer had a number averaged molar mass of $10.6 \cdot 10^3$ g/mol and a degree of functionalization of > 99%.

The viscosity of the resins was determined in rheology experiments (supplementary information, figure SI2). Between a shear rate of 0.01 and 100 s^{-1} the viscosity of the LowEC, MidEC and HighEC resins was between $42 \cdot 10^3$ and 60 Pa·s, $7 \cdot 10^3$ and 4.5 Pa·s and 7.9 and 0.08 Pa·s respectively. Although the increasing EC content decreased resin viscosity, all resins were shear thinning.

The melting and crystallization temperatures of the resins were determined in DSC experiments (supplementary information, figure SI3). The melting temperature of the LowEC, MidEC and HighEC resins was 23.7 ± 0.3 °C, 34.8 ± 1.0 °C and 41.7 ± 0.3 °C, respectively. The crystallization temperature of the MidEC and HighEC resins was 12.9 ± 7.5 °C and 26.7 ± 2.6 °C. No crystallization peak was found for the LowEC resin in DSC experiments. To ensure that the resins could be readily cast, temperatures were applied at or well above their melting temperatures depending on their viscosity. The resins were thereafter cooled to temperatures below their crystallization temperature to ensure

the formation of EC crystals. In case of the LowEC resin a cooling temperature of −25 °C was applied for 2 h. Crystallization of EC was thereafter confirmed by a transition in appearance of the resin from glistening to matte.

The effective crystallization of EC in all resins after cooling was further confirmed by the porosity of the resulting photo-crosslinked composite films after EC extraction. The porosity was determined gravimetrically and was 27 ± 3%, 52 ± 4% and 71 ± 5% for films prepared from LowEC, MidEC and HighEC resins respectively. Clearly, the porosity of the composites increased with increasing EC concentration in the resins, although porosities were lower than intended (equaling the 35, 60 and 85 vol% of EC in the LowEC, MidEC and HighEC resin, respectively). This may be caused by partial collapse of the pores after EC extraction.

Fig. 1 depicts SEM and AFM images of the surface of the composites as well as SEM images of the cross-section, depicting the presence of pores in the composites.

In Fig. 1a and d it is apparent that the composites with 27% porosity possessed a relatively low amount of pores and several shallow craters on its surface. In the cross-section only very small, isolated pores with a width of less than 0.5 μm could be found in high magnification images (insert Fig. 1d). Composites with 52% and 71% porosity possessed a rougher surface morphology due to the larger amount of pores on the surface, as can be seen in Fig. 1b and c. Furthermore, the cross-sections of these composites contained pores throughout as is shown in Fig. 1e and f. The orientation of the pores in these composites was heterogeneous through the cross-section as well as on the surface.

From SEM images, the pore width of pores on the composite film surfaces and in the cross-sections was determined. Table 3 gives an

Table 3

Pore width distribution on the surface and in the cross-section of porous composite films.

Location	Pore width	Porosity 27%	52%	71%
Surface	Average (μm)	8.6	4.7	8.5
	Minimum (μm)	2.4	0.3	0.9
	Maximum (μm)	44.8	24.5	105
Cross-section	Average (μm)	0.11	12.4	19.7
	Minimum (μm)	0.02	1.8	0.3
	Maximum (μm)	0.47	54.9	120

overview of the pore width distribution of the composite films.

From the pore width distributions given in table 3 it can be seen that the average pore widths on the surface of the films are close although the distribution is different. Composites with 52% porosity possess the most confined distribution between 0.3 and 24.5 μm, whereas composites with 71% porosity possess the widest distribution with some pores exceeding 100 μm in width. Nonetheless, the majority of the pores (>90% by number) on all films were smaller than 20 μm in width and no significant differences between the size distributions were found. These values indicate that the majority of pores at the surface of all films allow only for a limited cell infiltration and cells will mainly interact with the composites at their outer surface[4,5], sensing similar pore sizes. In the cross-section of the composite films, the pore width increases and the size distribution increases with increasing porosity (and thus with the amount of EC used during preparation). The content of EC, along with the applied cooling rate, influences the nucleation and crystal growth rate of EC crystals upon cooling of the composite resins. This directly affects the size of the resulting EC crystals[52]. The differences in pore
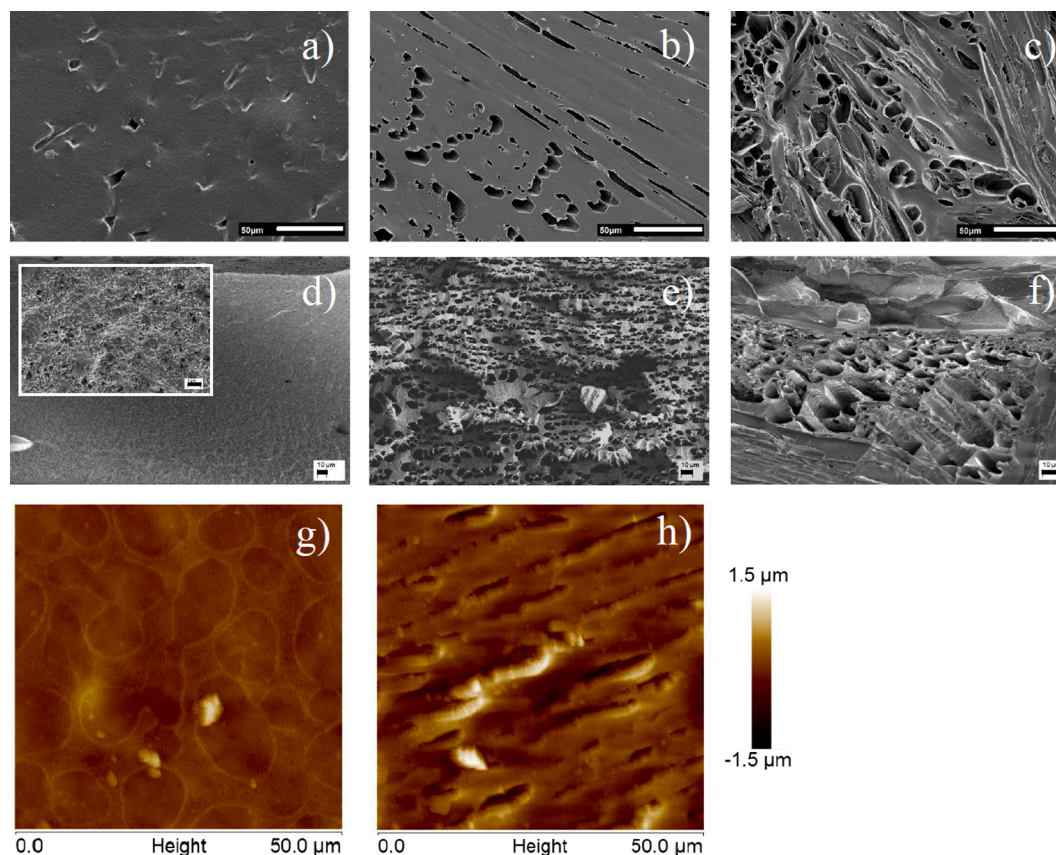

Fig. 1. SEM images of the surface (a, b, c) and cross-section (d, e, f) of composite films with 27% (a, d), 52% (b, e) and 71% (c, f) porosity and AFM images of composite films with 27% (g) and 52% (h) porosity. The surface of composites with 71% porosity could not be analysed by AFM due to large height differences. Composites with 27%, 52% and 71% porosity were prepared from LowEC, MidEC and HighEC resin respectively. Scale bars a, b, c = 50 μm; scale bars d, e, f = 10 μm; scale bar insert d = 1 μm.

width distribution in the resulting photo-crosslinked composites may therefore be minimized by controlling the cooling rate of the resins carefully.

In Fig. 1g and 1 h AFM images of composites with 27% and 52% porosity are shown and it was observed that roughness increased with increasing porosity. From the AFM images an R_a of 82 ± 11 nm and R_q of 107 ± 21 nm were determined for composites with 27% porosity. The R_a of composites with 52% porosity was 213 ± 49 nm and the R_q value was 279 ± 60 nm. These results suggest that with increasing porosity not only nano-scale height features increase on the surface (R_a), but also the height differences between them (R_q); implying more irregular surfaces on the nano-scale are present on the higher porosity composites.

The porous composite films were further characterized in terms of their nHA content and their mechanical properties. An overview of these characteristics is given in table 4.

The nHA content in the composites was determined to be between 40 and 50 wt% by TGA (supplementary information figure SI4). Differences observed in the nHA content did not correlate to the EC contents in the resins, indicating that it did not significantly affect nHA incorporation or distribution.

From tensile mechanical properties in table 4 it is clear that the composites become less stiff as their porosity is increased. Composites with 27% porosity possess a relatively high stiffness, ultimate tensile strength and toughness. Composites with 71% porosity possess an almost twenty-fold lower stiffness and ultimate tensile strength and hundred-fold lower toughness. As cells will mainly interact at the surface of our composites due to the small pore sizes and the possibility for cells to span these pores[53], we hypothesize that these changes in tensile stiffness can be perceived by cells seeded on the composites[54].

A calcium release experiment was performed in a formic acid buffer (pH = 4.5) to obtain an indication of the effect of the different porosities on the calcium release. Fig. 2 shows the determined calcium release profile.

In Fig. 2a it can be seen that calcium release from all porous composites is similar. Over 30 days there was no significant difference in the amount of calcium released. The amount of composite per unit volume in samples with high porosity is much lower than in those with low porosity however. Thus, when comparing the amount of calcium ions released to the total initial nHA content in each composite film, it is clear that the composite with 71% porosity more rapidly releases its calcium content compared to the other composites. This is illustrated in Fig. 2b. This may explain the similar overall release rates observed in Fig. 2a. Given this similarity, it is unlikely that it will affect osteogenic differentiation of hBMSCs.

The protein adsorption on the porous composites films was determined as well, and it was found that the porous composites with 27%, 52% and 71% porosity had a protein adhesion of 1.3 ± 0.3, 8.6 ± 1.4 and 15.6 ± 2.2 µg/sample respectively. This can be expected as the surface area of the composites increases with increasing porosity and it may be beneficial for cell adherence and differentiation[44,46].

3.2. Proliferation and osteogenic differentiation of hBMSCs on porous composite films

An adhesion study of hBMSCs on the composite films was performed to investigate the effect of the varying porosity and surface morphology on the initial binding of cells on the composites. In Fig. 3a the amount of DNA of adhering cells per composite film sample is shown. As a positive control TCPS is shown as well. On all films cells were adhering well. Although significant differences in adherence on the composites with varying porosity were observed initially, these differences became non-significant over prolonged adhesion times. After 60 min of incubation, cells on all films showed similar adherence as on the TCPS control. Only on composites with 27% porosity the adhesion is slightly lower than on the other composites.

Continued cell proliferation was monitored by their metabolic activity. It is shown in Fig. 3b, that the hBMSCs grow well as their metabolic activity increases significantly over time up to 13 days of culture (significant differences between time points were assessed by a two-tailed Welch's *t*-test; results are not indicated in figure). Thereafter a decrease of the metabolic activity was observed on films with 27 and 52% porosity whereas the metabolic activity remained *quasi* constant on films with 71% porosity and the TCPS control. This may be related to the confluence as well as the differentiation of the cells[55]. The metabolic activity was initially highest on the composite with 27% porosity and was comparable to that of the TCPS control. After 28 days of culture the lowest average metabolic activity was observed on this composite, although no significance difference was found with the other porous composites.

Good adhesion and proliferation of the hBMSCs on all composites was furthermore shown by Live/Dead® staining and SEM images. Fig. 4a, b and c show the Live/Dead® staining of cells after one day of culture. On all porous composites the cells were mainly alive and only a few dead cells were observed. After 28 days of culture all porous composites were covered in live cells and few dead cells as shown in Fig. 4d, e and f. This was confirmed by SEM images of the cell-covered films after 28 days of culture, which are shown in Fig. 4g, h and i. In high magnification SEM images in Fig. 4j, k and l, calcium phosphate deposits can be observed which are evident of the osteogenic differentiation of the hBMSCs[44,56]. Please note that we have refrained from attempting to analyse calcium production from these images, as they do not provide for an accurate quantification. ARS staining was used for this purpose instead (*v.i.*).

Two distinguishing observations were made for the cells cultured on composites with 71% porosity. In the Live/Dead® staining images after 1 day of culture it was seen that the cells tended to align along the length of the pore channels parallel to the surface on these composites (in subsequent days this could not be observed due to cell overgrowth obscuring underlying pores). To a lesser extent this was also seen on the composites with 52% porosity. Additionally, in the SEM images after 28 days of culture it was observed that cells were unable to traverse some of the large pore channels present on the surface of the composites with 71% porosity. Similar behaviour has been observed for osteoblasts grown on porous titanium[53], and was ascribed to the cells' inability to span large pores by elongation. In these cases cells tend to grow along the edges of larger pores (>100 µm) or into the pores when sufficiently large (>200 µm). This may have a profound implication for the differentiation of the hBMSCs on the 71% porous composites reported here, as the larger pores will affect the cell spreading and their morphology, which plays a pivotal role in cell differentiation[7,13,14].

As was expected from the pore sizes measured at the surface of the films (table 3), no evidence of cell infiltration into the porous films was found during Live/Dead® imaging using fluorescent confocal microscopy (data not shown).

To investigate the extent of osteogenic differentiation of the hBMSCs on the porous composites, the ALP ezyme activity and calcium production of the cells was quantified. Both assessments are depicted in
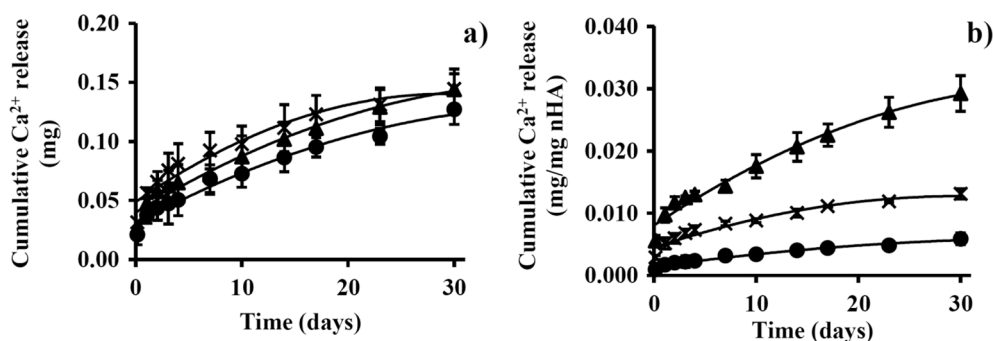
Table 4
Characteristics of the prepared porous composite films.

Property	Porosity		
	27%	52%	71%
nHA content (wt.%)	41.2 ± 0.2	48.8 ± 2.2	40.3 ± 1.2
E modulus (MPa)	67.4 ± 3.5	28.0 ± 4.3	3.53 ± 1.37
Yield strength (N/mm^2)	1.8 ± 0.1	0.8 ± 0.1	0.12 ± 0.04
Yield strain (%)	2.4 ± 0.03	2.7 ± 0.07	3.2 ± 0.4
Ultimate tensile strength (N/mm^2)	5.3 ± 1.2	1.9 ± 0.2	0.26 ± 0.05
Strain at break (%)	66.8 ± 23.8	24.1 ± 2.3	13.4 ± 4.2
Toughness (N/mm^2)	263 ± 134	31.2 ± 5.2	2.18 ± 0.74

Fig. 2. Cumulative calcium release from porous composite films (a) and cumulative release relative to the total nHA content in the films (b) with 27% (dots), 52% (crosses) and 71% (triangles) porosity. Lines in graphs are shown to guide the eye.
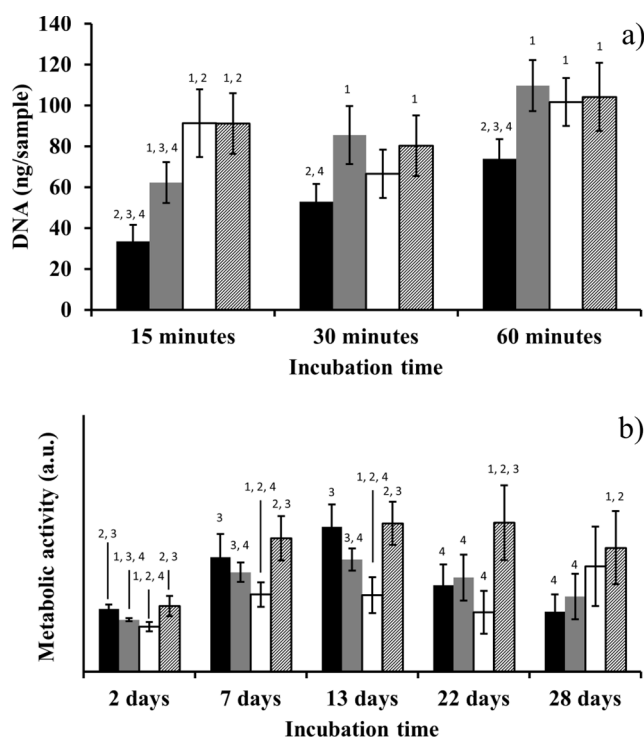

Fig. 3. Cell adhesion expressed in DNA content of adhering cells per sample (a) and the evolution of the metabolic activity of hBMSCs over time (b) on porous composite films with 27% (black bars), 52% (grey bars) and 71% (white bars) porosity and TCPS (bars with black shading). Numbers above bars indicate significant differences in comparison with porous composite films with 27% (1), 52% (2) and 71% (3) porosity and with TCPS (4) within each time point. An absence of numbering indicates the lack of a significant difference in comparison with any of the other samples.

Fig. 5.

The ALP activity shown in Fig. 5a is similar on all sample types and between 15 and 23 days of culture, the ALP activity on all samples including the TCPS control decreased significantly. It is known that during the osteogenic differentiation of hBMSCs, the cells proliferate after which an initial increase of ALP activity occurs during differentiation. This is followed by a decrease as the differentiated cells excrete a mineralized matrix[57]. During the peaking of ALP activity, the enzyme hydrolyses organic phosphates to form pyrophosphates that promote precipitation of calcium phosphates extracellularly[30,58]. This peaking of ALP activity is thus an early marker for cell differentiation and essential to subsequent mineralization. Moreover, the moment at which the peak in ALP activity occurs, is indicative of the tendency of the cells to either proliferate (late peaking) or differentiate (early peaking)[57].
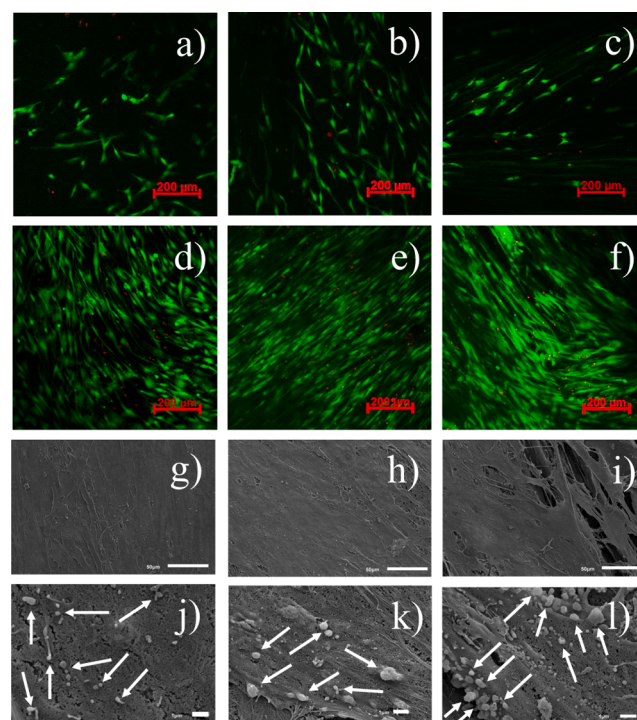

Fig. 4. Live/Dead® images after 1 day (a, b and c) and 28 days (d, e and f) of culture, cell-covered composite film surfaces (g, h and i) imaged by SEM after 28 days of culture and high magnification SEM images of the cell surface after 28 days of culture (j, k and l) on composites with 27% (a, d, g and j), 52% (b, e, h and k) and 71% (c, f, i and l) porosity. Arrows in j, k and l point out calcium phosphate deposits. Scale bars g, h, i = 50 μm; scale bars j, k, l = 1 μm. All images depicted are from cells of a single donor.

In our experiments, the actual peak in ALP activity is not observed and no significant differences between the cells on the different sample types were found. However, the decrease of the ALP activity did coincide with the observed decrease or levelling of the metabolic activity between 13 and 22 days of culture (Fig. 3b) which can be related to the lower metabolic activity of cells in the osteogenic lineage compared to hBMSCs [55]. This decrease or levelling of the metabolic activity was not observed at earlier time points, implying that ALP activity may peak between 7 and 22 days of culture. Since the ALP activity of the cells on the various porous composites can peak at different time points within this range, we are not able to directly relate it to differences in the tendency for osteogenic differentiation of the cells[5,57]. Determination of the ALP activity over multiple early time points in future experiments may yield a kinetic description of the development of ALP activity. We expect that this would show clear differences in its development
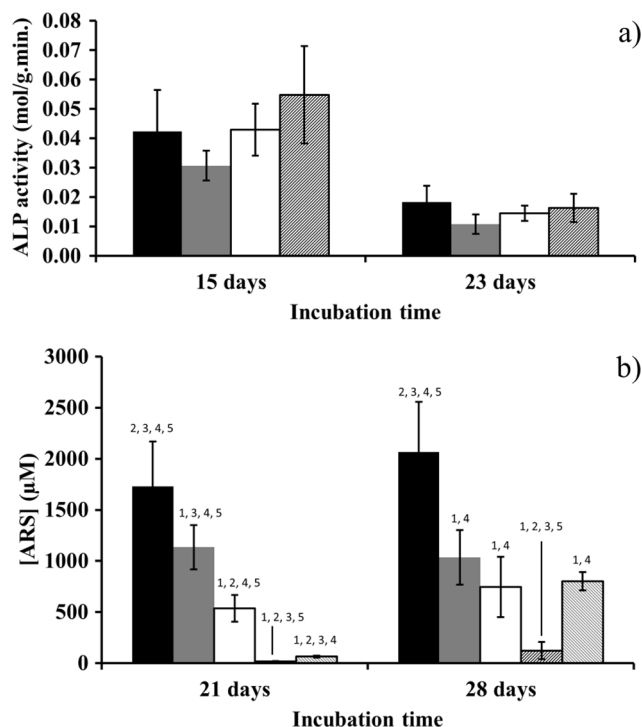
Fig. 5. Quantification of the ALP activity of cells on porous composites (a) and ARS concentration on composites (b) with 27% (black bars), 52% (grey bars) and 71% (white bars) porosity, TCPS (bars with black shading) and Thermanox™ (bars with grey shading). Numbers above bars indicate significant differences in comparison with porous composite films with 27% (1), 52% (2) and 71% (3) porosity and with TCPS (4) or Thermanox™ (5) within each time point. An absence of numbering indicates the lack of a significant difference in comparison with any of the other samples.

between the cells cultured on the different films. The finalization of ALP peaking in concurrence with a decreasing metabolic activity nonetheless serves as confirmation of the osteogenic differentiation of cells on the porous composite films.

The ARS staining quantification given in Fig. 5b, shows that the cells produce significant amounts of calcium on the porous composites compared to the TCPS and Thermanox™ controls. The amount of calcium produced decreased significantly with an increasing porosity and between 21 and 28 days the amount of additional calcium produced by cells on the porous composites was not significant. On day 28 of culture, the amount of calcium produced by the cells is similar to the Thermanox™ control on composites with 52% and 71% porosity. On composites with 27% porosity, the calcium production of the cells is significantly higher. The enhanced calcium production on the 27% porosity composites compared to those with higher porosity and the controls, indicates the strong maturation of the hBMSCs into the osteogenic lineage on the lower porosity composites.

3.3. General discussion

In this work, we have demonstrated that using TIPS with varying amounts of a crystallisable solvent allows for the modification of microscale porosity of photo-crosslinked PTMC and nHA composites. As a result, these composites have different micro- and nano-topologies as was demonstrated by SEM and AFM imaging. In previous works, shallow micro-scale features in the size range of several microns to hundreds of microns and roughness parameters in the micrometer range were shown to drive cell aggregation and differentiation as opposed to proliferation [23], and nano-scale roughness features were shown to allow for an enhanced protein adhesion and circulation at material surfaces and

enhance cell adhesion and their spreading[59,60]. In this work we observed an enhanced nano-scale roughness on the microporous composites as their porosity was increased. The increasing porosity and higher surface roughness allowed for a higher protein adhesion, which has been described in literature as beneficial for cell adhesion and their differentiation[61]. Indeed, more cells initially adhered on the higher porosity composites compared to the lower porosity ones. Changes in nano-scale features need to be corroborated by beneficial changes in micro-scale features for an effective enhancement of osteogenic differentiation, however[8–10]. Changes in microscale features of our composites (Fig. 1, table 3) may not be complementary to the enhanced surface roughness on the nanoscale and ensuing protein adsorption. We observed that with increasing porosity, the surfaces of the composites in this work change topology from shallow craters to deep and densely packed pore channels. A reduced differentiation potential of hBMSCs on composites with pores in a size range of 1 to 50 μm and an increasing porosity has been described in literature before[2,19]. It is thought that this is caused by an enhanced cell proliferation and decreased aggregation on materials with increasing porosity[2,18,19,62]. It is therefore likely that such micro-scale topological changes on our composites with increasing porosity outweigh the increasing nano-scale roughness parameters.

Additionally, with increasing porosity a reduction in tensile stiffness and toughness of our composites was observed. Although macroscopic indicators of mechanical properties, the width of the majority of pores in this work is sufficiently small for cells to span multiple pores[53]. Through the cells' contractile forces applied on their substrate, the changes in tensile mechanical properties could therefore be sensed by the cells. The difference in tensile stiffness reported here (ranging from 3.5 to 67 MPa for a porosity of 71 to 27%, respectively) can be sufficient to affect osteogenic differentiation. Indeed, in other works it has been demonstrated that an increase in the tensile stiffness of randomly oriented, fibrous collagen films from 10 MPa to 100 MPa may favour osteogenic differentiation of mesenchymal stem cells cultured on their surface[54].

The effect of these results is corroborated by the difference we observed in mineralization on the composites. Although we were not able to observe a peak in ALP activity, the high calcium production by cells on lower porosity composites suggests an earlier or stronger peaking (higher ALP concentrations) of ALP activity on these composites compared to higher porosity ones[30]. These results can be directly related to the differences in micro-scale morphology of the composites and their reduced stiffness. As cells are adapting their morphology to their substrate and while the cells probe its mechanical properties, their cytoskeletal tension is modified accordingly[63]. For differentiation into the osteogenic lineage, a relatively high tension is required which cannot be achieved if cell spreading is impaired or when the substrate for attachment is not sufficiently rigid. This, in turn will not activate RUNX2, the first transcription factor necessary for osteoblastic differentiation. Whether this is the case on our microporous composites will need to be confirmed in future experiments that include gene expression experiments.

Also in other works it has been shown that an increasing porosity reduces osteogenic differentiation *in vitro*, but that it can still be beneficial for bone restoration *in vivo*[18,19,64]. Therefore, *in vivo* experiments are required to understand the effect of increasing micro-scale porosity in photo-crosslinked PTMC and nHA composites on bone restoration efficacy. Currently we have already prepared three-dimensional implant structures with resins described here and a low temperature extrusion-based additive manufacturing technique. A description of these structures is given in the supplementary information (Section SI2) of this work. These structures possess a designed porosity on a macroscale (>300 μm) in combination with the microscale porosity reported here. As mentioned in the introduction of this work, the macroscale porosity allows for infiltration of bone tissue throughout the scaffolds whereas the microscale porosity can be beneficial for nutrient

and waste transport whilst not infiltrated by cells and *de novo* tissue [4,5,40]. We hypothesize that such a structure will enhance bone ingrowth as the microscale porosity is increased. Although this seems contradictory to the *in vitro* cell differentiation results presented in this work, this effect has indeed been demonstrated in past publications[19].

4. Conclusions

In this work we have shown that resins based on PTMC-MA, nHA and EC are suitable for the preparation of porous composites with varying porosity. The resin viscosity and phase separation temperatures can be adjusted by controlling the EC concentration. Using this phase separation and photo-crosslinking, the EC concentration can directly affect the porosity, pore size and mechanical properties of the composites. An increasing porosity affected the surface morphology and reduced the stiffness of the porous composites. These modifications reduce the ability of hBMSCs to differentiate into the osteogenic lineage as was shown by the calcium deposition of the cells. This is in line with what has been reported in literature before on the *in vitro* differentiation of hBMSCs on porous materials. Reduced cell aggregation, inability to adapt a favourable morphology for osteogenic differentiation and low stiffness of the porous composite may be the cause for this effect. Implantation experiments are required to assess the effect of porosity in porous, photo-crosslinked PTMC-MA/nHA structures on the regeneration of bony defects.

CRediT authorship contribution statement

Mike A. Geven: Conceptualization, Experimental work, Writing. **Anna Lapomarda:** Experimental work, Writing. **Olivier Guillaume:** Conceptualization, Supervision. **Christoph M. Sprecher:** Supervision. **David Eglin:** Funding acquisition, Project administration, Conceptualization, Supervision. **Giovanni Vozzi:** Conceptualization, Supervision. **Dirk W. Grijpma:** Funding acquisition, Project administration, Conceptualization, Supervision, Corrections.

Declaration of Competing Interest

The authors declared that there is no conflict of interest.

Acknowledgements

Appendix A. Supplementary data

Supplementary data to this article can be found online at https://doi.org/10.1016/j.eurpolymj.2021.110335.

References

[1] F.A. Akin, H. Zreiqat, S. Jordan, M.B. Wijesundara, L. Hanley, Preparation and analysis of macroporous TiO2 films on Ti surfaces for bone-tissue implants, J. Biomed. Mater. Res. 57 (4) (2001) 588–596.

[2] Y. Takahashi, Y. Tabata, Effect of the fiber diameter and porosity of non-woven PET fabrics on the osteogenic differentiation of mesenchymal stem cells, J. Biomater. Sci. Polym. Ed. 15 (1) (2004) 41–57.

[3] G. Akay, M.A. Birch, M.A. Bokhari, Microcellular polyHIPE polymer supports osteoblast growth and bone formation in vitro, Biomaterials 25 (18) (2004) 3991–4000.

[4] C.M. Murphy, M.G. Haugh, F.J. O'Brien, The effect of mean pore size on cell attachment, proliferation and migration in collagen-glycosaminoglycan scaffolds for bone tissue engineering, Biomaterials 31 (3) (2010) 461–466.

[5] A. Salerno, D. Guarnieri, M. Iannone, S. Zeppetelli, P.A. Netti, Effect of micro- and macroporosity of bone tissue three-dimensional-poly(epsilon-caprolactone) scaffold on human mesenchymal stem cells invasion, proliferation, and differentiation in vitro, Tissue Eng. Part A 16 (8) (2010) 2661–2673.

[6] M.E. Gomes, H.L. Holtorf, R.L. Reis, A.G. Mikos, Influence of the porosity of starch-based fiber mesh scaffolds on the proliferation and osteogenic differentiation of bone marrow stromal cells cultured in a flow perfusion bioreactor, Tissue Eng. 12 (4) (2006) 801–809.

[7] L. Zhao, L. Liu, Z. Wu, Y. Zhang, P.K. Chu, Effects of micropitted/nanotubular titania topographies on bone mesenchymal stem cell osteogenic differentiation, Biomaterials 33 (9) (2012) 2629–2641.

[8] R.A. Gittens, T. McLachlan, R. Olivares-Navarrete, Y. Cai, S. Berner, R. Tannenbaum, Z. Schwartz, K.H. Sandhage, B.D. Boyan, The effects of combined micron-/submicron-scale surface roughness and nanoscale features on cell proliferation and differentiation, Biomaterials 32 (13) (2011) 3395–3403.

[9] J. Zhang, X. Luo, D. Barbieri, A.M. Barradas, J.D. de Bruijn, C.A. van Blitterswijk, H. Yuan, The size of surface microstructures as an osteogenic factor in calcium phosphate ceramics, Acta Biomater. 10 (7) (2014) 3254–3263.

[10] D.D. Deligianni, N.D. Katsala, P.G. Koutsoukos, Y.F. Missirlis, Effect of surface roughness of hydroxyapatite on human bone marrow cell adhesion, proliferation, differentiation and detachment strength, Biomaterials 22 (1) (2001) 87–96.

[11] I. Wall, N. Donos, K. Carlqvist, F. Jones, P. Brett, Modified titanium surfaces promote accelerated osteogenic differentiation of mesenchymal stromal cells in vitro, Bone 45 (1) (2009) 17–26.

[12] P. Muller, U. Bulnheim, A. Diener, F. Luthen, M. Teller, E.D. Klinkenberg, H. G. Neumann, B. Nebe, A. Liebold, G. Steinhoff, J. Rychly, Calcium phosphate surfaces promote osteogenic differentiation of mesenchymal stem cells, J. Cell Mol. Med. 12 (1) (2008) 281–291.

[13] L. Xia, K. Lin, X. Jiang, B. Fang, Y. Xu, J. Liu, D. Zeng, M. Zhang, X. Zhang, J. Chang, Z. Zhang, Effect of nano-structured bioceramic surface on osteogenic differentiation of adipose derived stem cells, Biomaterials 35 (30) (2014) 8514–8527.

[14] F.F.B. Hulshof, B. Papenburg, A. Vasilevich, M. Hulsman, Y. Zhao, M. Levers, N. Fekete, M. de Boer, H. Yuan, S. Singh, N. Beijer, M.A. Bray, D.J. Logan, M. Reinders, A.E. Carpenter, C. van Blitterswijk, D. Stamatialis, J. de Boer, Mining for osteogenic surface topographies: In silico design to in vivo osseo-integration, Biomaterials 137 (2017) 49–60.

[15] K. Chatterjee, S. Lin-Gibson, W.E. Wallace, S.H. Parekh, Y.J. Lee, M.T. Cicerone, M. F. Young, C.G. Simon Jr., The effect of 3D hydrogel scaffold modulus on osteoblast differentiation and mineralization revealed by combinatorial screening, Biomaterials 31 (19) (2010) 5051–5062.

[16] J.H. Wen, L.G. Vincent, A. Fuhrmann, Y.S. Choi, K.C. Hribar, H. Taylor-Weiner, S. Chen, A.J. Engler, Interplay of matrix stiffness and protein tethering in stem cell differentiation, Nat. Mater. 13 (10) (2014) 979–987.

[17] J. Nam, J. Johnson, J.J. Lannutti, S. Agarwal, Modulation of embryonic mesenchymal progenitor cell differentiation via control over pure mechanical modulus in electrospun nanofibers, Acta Biomater. 7 (4) (2011) 1516–1524.

[18] D.W. Hutmacher, J.T. Schantz, C.X. Lam, K.C. Tan, T.C. Lim, State of the art and future directions of scaffold-based bone engineering from a biomaterials perspective, J Tissue Eng Regen Med 1 (4) (2007) 245–260.

[19] V. Karageorgiou, D. Kaplan, Porosity of 3D biomaterial scaffolds and osteogenesis, Biomaterials 26 (27) (2005) 5474–5491.

[20] C. Sanchez, B. Julián, P. Belleville, M. Popall, Applications of hybrid organic–inorganic nanocomposites, J. Mater. Chem. 15 (35–36) (2005) 3559–3592.

[21] G.L. Koons, M. Diba, A.G. Mikos, Materials design for bone-tissue engineering, Nat. Rev. Mater. 5 (8) (2020) 584–603.

[22] M.S. Saveleva, K. Eftekhari, A. Abalymov, T.E.L. Douglas, B. V. Parakhonskiy, A.G. Skirtach, Hierarchy of Hybrid Materials-The Place of Inorganics-in-Organics in it Their Composition and Applications, Front Chem 7 (2019) 179.

[23] A.L. Raines, R. Olivares-Navarrete, M. Wieland, D.L. Cochran, Z. Schwartz, B. D. Boyan, Regulation of angiogenesis during osseointegration by titanium surface microstructure and energy, Biomaterials 31 (18) (2010) 4909–4917.

[24] I.H. Kim, J.S. Son, T.Y. Kwon, K.H. Kim, Effect of Atmospheric Plasma Treatment to Titanium Surface on Initial Osteoblast-Like Cell Spreading, J. Nanosci. Nanotechnol. 15 (1) (2015) 134–137.

[25] H.S. Roh, S.C. Jung, M.S. Kook, B.H. Kim, In vitro study of 3D PLGA/n-HAp/beta-TCP composite scaffolds with etched oxygen plasma surface modification in bone tissue engineering, Appl. Surf. Sci. 388 (2016) 321–330.

[26] A. Yeo, W.J. Wong, H.H. Khoo, S.H. Teoh, Surface modification of PCL-TCP scaffolds improve interfacial mechanical interlock and enhance early bone formation: an in vitro and in vivo characterization, J Biomed Mater Res A 92 (1) (2010) 311–321.

[27] H.T. Liao, M.Y. Lee, W.W. Tsai, H.C. Wang, W.C. Lu, Osteogenesis of adipose-derived stem cells on polycaprolactone-beta-tricalcium phosphate scaffold fabricated via selective laser sintering and surface coating with collagen type I, J Tissue Eng Regen Med 10 (10) (2016) E337–E353.

[28] M.T. Arafat, C.X. Lam, A.K. Ekaputra, S.Y. Wong, X. Li, I. Gibson, Biomimetic composite coating on rapid prototyped scaffolds for bone tissue engineering, Acta Biomater. 7 (2) (2011) 809–820.

[29] T. Egghe, P. Cools, J.F.R. Van Guyse, M. Asadian, D. Khalenkow, A. Nikiforov, H. Declercq, A.G. Skirtach, R. Morent, R. Hoogenboom, N. De Geyter, Water-Stable

Plasma-Polymerized N, N-Dimethylacrylamide Coatings to Control Cellular Adhesion, ACS Appl. Mater. Interfaces 12 (2) (2020) 2116–2128.

[30] A. Sengottuvelan, P. Balasubramanian, J. Will, A.R. Boccaccini, Bioactivation of titanium dioxide scaffolds by ALP-functionalization, Bioact. Mater. 2 (2) (2017) 108–115.

[31] C. Muderrisoglu, M. Saveleva, A. Abalymov, L. Van der Meeren, A. Ivanova, V. Atkin, B. Parakhonskiy, A.G. Skirtach, Nanostructured Biointerfaces Based on Bioceramic Calcium Carbonate/Hydrogel Coatings on Titanium with an Active Enzyme for Stimulating Osteoblasts Growth, Adv. Mater. Interfaces 5 (19) (2018).

[32] B. van Bochove, D.W. Grijpma, Mechanical properties of porous photo-crosslinked poly(trimethylene carbonate) network films, Eur. Polym. J. 143 (2021), 110223.

[33] C. Ruiz-Aguilar, U. Olivares-Pinto, R.A.L. Drew, E.A. Aguilar-Reyes, I. Alfonso, Porogen Effect on Structural and Physical Properties of β-TCP Scaffolds for Bone Tissue Regeneration, IRBM (2020).

[34] E. Zant, M.M. Blokzijl, D.W. Grijpma, A Combinatorial Photocrosslinking Method for the Preparation of Porous Structures with Widely Differing Properties, Macromol Rapid Comm 36 (21) (2015) 1902–1909.

[35] O. Guillaume, M.A. Geven, C.M. Sprecher, V.A. Stadelmann, D.W. Grijpma, T. T. Tang, L. Qin, Y. Lai, M. Alini, J.D. de Bruijn, H. Yuan, R.G. Richards, D. Eglin, Surface-enrichment with hydroxyapatite nanoparticles in stereolithography-fabricated composite polymer scaffolds promotes bone repair, Acta Biomater. 54 (2017) 386–398.

[36] Z. Guo, D. Grijpma, A. Poot, Leachable Poly(Trimethylene Carbonate)/CaCO3 Composites for Additive Manufacturing of Microporous Vascular Structures, Materials (Basel) 13 (15) (2020).

[37] M.A. Geven, C. Sprecher, O. Guillaume, D. Eglin, D.W. Grijpma, Micro-porous composite scaffolds of photo-crosslinked poly(trimethylene carbonate) and nano-hydroxyapatite prepared by low-temperature extrusion-based additive manufacturing, Polym. Adv. Technol. 28 (10) (2017) 1226–1232.

[38] Y. Kuboki, Q. Jin, H. Takita, Geometry of carriers controlling phenotypic expression in BMP-induced osteogenesis and chondrogenesis, J Bone Joint Surg Am 83-A Suppl 1 (Pt 2) (2001) S105–S115.

[39] Y. Kuboki, Q. Jin, M. Kikuchi, J. Mamood, H. Takita, Geometry of artificial ECM: sizes of pores controlling phenotype expression in BMP-induced osteogenesis and chondrogenesis, Connect. Tissue Res. 43 (2–3) (2002) 529–534.

[40] S. Bose, M. Roy, A. Bandyopadhyay, Recent advances in bone tissue engineering scaffolds, Trends Biotechnol. 30 (10) (2012) 546–554.

[41] S. Tarafder, V.K. Balla, N.M. Davies, A. Bandyopadhyay, S. Bose, Microwave-sintered 3D printed tricalcium phosphate scaffolds for bone tissue engineering, J Tissue Eng Regen Med 7 (8) (2013) 631–641.

[42] P. Habibovic, K. de Groot, Osteoinductive biomaterials–properties and relevance in bone repair, J Tissue Eng Regen Med 1 (1) (2007) 25–32.

[43] A.J. Engler, S. Sen, H.L. Sweeney, D.E. Discher, Matrix elasticity directs stem cell lineage specification, Cell 126 (4) (2006) 677–689.

[44] O. Guillaume, M.A. Geven, D.W. Grijpma, T.T. Tang, L. Qin, Y.X. Lai, H. Yuan, R. G. Richards, D. Eglin, Poly(trimethylene carbonate) and nano-hydroxyapatite porous scaffolds manufactured by stereolithography, Polym. Adv. Technol. 28 (10) (2017) 1219–1225.

[45] O. Guillaume, M.A. Geven, V. Varjas, P. Varga, D. Gehweiler, V.A. Stadelmann, T. Smidt, S. Zeiter, C. Sprecher, R.R.M. Bos, D.W. Grijpma, M. Alini, H. Yuan, G. R. Richards, T. Tang, L. Qin, L. Yuxiao, P. Jiang, D. Eglin, Orbital floor repair using patient specific osteoinductive implant made by stereolithography, Biomaterials 233 (2020), 119721.

[46] R.Z. LeGeros, Calcium phosphate-based osteoinductive materials, Chem. Rev. 108 (11) (2008) 4742–4753.

[47] D. Barbieri, A.J. Renard, J.D. de Bruijn, H. Yuan, Heterotopic bone formation by nano-apatite containing poly(D, L-lactide) composites, Eur Cell Mater 19 (2010) 252–261.

[48] M.A. Geven, D. Barbieri, H. Yuan, J.D. de Bruijn, D.W. Grijpma, Preparation and mechanical properties of photo-crosslinked poly(trimethylene carbonate) and nano-hydroxyapatite composites, Clin. Hemorheol. Microcirc. 60 (1) (2015) 3–11.

[49] M.A. Geven, V. Varjas, L. Kamer, X. Wang, J. Peng, D. Eglin, D.W. Grijpma, Fabrication of patient specific composite orbital floor implants by stereolithography, Polym. Adv. Technol. 26 (12) (2015) 1433–1438.

[50] E.S. Gadelmawla, M.M. Koura, T.M.A. Maksoud, I.M. Elewa, H.H. Soliman, Roughness parameters, J. Mater. Process. Technol. 123 (1) (2002) 133–145.

[51] M. Herrmann, J.J. Bara, C.M. Sprecher, U. Menzel, J.M. Jalowiec, R. Osinga, A. Scherberich, M. Alini, S. Verrier, Pericyte plasticity - comparative investigation of the angiogenic and multilineage potential of pericytes from different human tissues, Eur Cell Mater 31 (2016) 236–249.

[52] R. Zhang, P.X. Ma, Poly(alpha-hydroxyl acids)/hydroxyapatite porous composites for bone-tissue engineering. I. Preparation and morphology, J. Biomed. Mater. Res. 44 (4) (1999) 446–455.

[53] W. Xue, B.V. Krishna, A. Bandyopadhyay, S. Bose, Processing and biocompatibility evaluation of laser processed porous titanium, Acta Biomater. 3 (6) (2007) 1007–1018.

[54] A. Islam, T. Mbimba, M. Younesi, O. Akkus, Effects of substrate stiffness on the tenoinduction of human mesenchymal stem cells, Acta Biomater. 58 (2017) 244–253.

[55] M. Westhrin, M. Xie, M.O. Olderoy, P. Sikorski, B.L. Strand, T. Standal, Osteogenic differentiation of human mesenchymal stem cells in mineralized alginate matrices, PLoS ONE 10 (3) (2015) e0120374.

[56] A. Martins, A.R. Duarte, S. Faria, A.P. Marques, R.L. Reis, N.M. Neves, Osteogenic induction of hBMSCs by electrospun scaffolds with dexamethasone release functionality, Biomaterials 31 (22) (2010) 5875–5885.

[57] E. Birmingham, G.L. Niebur, P.E. McHugh, G. Shaw, F.P. Barry, L.M. McNamara, Osteogenic differentiation of mesenchymal stem cells is regulated by osteocyte and osteoblast cells in a simplified bone niche, Eur Cell Mater 23 (2012) 13–27.

[58] E.E. Golub, G. Harrison, A.G. Taylor, S. Camper, I.M. Shapiro, The role of alkaline phosphatase in cartilage mineralization, Bone and Mineral 17 (2) (1992) 273–278.

[59] M.J. Biggs, R.G. Richards, N. Gadegaard, R.J. McMurray, S. Affrossman, C. D. Wilkinson, R.O. Oreffo, M.J. Dalby, Interactions with nanoscale topography: adhesion quantification and signal transduction in cells of osteogenic and multipotent lineage, J Biomed Mater Res A 91 (1) (2009) 195–208.

[60] M.J. Dalby, D. McCloy, M. Robertson, C.D. Wilkinson, R.O. Oreffo, Osteoprogenitor response to defined topographies with nanoscale depths, Biomaterials 27 (8) (2006) 1306–1315.

[61] K. Zhang, Y. Fan, N. Dunne, X. Li, Effect of microporosity on scaffolds for bone tissue engineering, Regen Biomater 5 (2) (2018) 115–124.

[62] J.M. Collins, P. Ayala, T.A. Desai, B. Russell, Three-dimensional culture with stiff microstructures increases proliferation and slows osteogenic differentiation of human mesenchymal stem cells, Small 6 (3) (2010) 355–360.

[63] Y.K. Wang, X. Yu, D.M. Cohen, M.A. Wozniak, M.T. Yang, L. Gao, J. Eyckmans, C. S. Chen, Bone morphogenetic protein-2-induced signaling and osteogenesis is regulated by cell shape, RhoA/ROCK, and cytoskeletal tension, Stem Cells Dev 21 (7) (2012) 1176–1186.

[64] T.D. Roy, J.L. Simon, J.L. Ricci, E.D. Rekow, V.P. Thompson, J.R. Parsons, Performance of degradable composite bone repair products made via three-dimensional fabrication techniques, J Biomed Mater Res A 66a(2) (2003) 283–291.